Computers and Structures 253 (2021) 106573

Contents lists available at ScienceDirect

Computers and Structures

journal homepage: www.elsevier.com/locate/compstruc

Nonlinear finite element models of reinforced concrete beams strengthened in bending with mechanically fastened aluminum alloy plates

Omar R. Abuodeh [a,c], Rami A. Hawileh [b,*], Jamal A. Abdalla [b]

[a] Glenn Department of Civil Engineering, Clemson University, Clemson, SC 29634, USA
[b] Department of Civil Engineering, American University of Sharjah, P.O.Box 26666, Sharjah, United Arab Emirates
[c] Formerly Graduate Student, Department of Civil Engineering, American University of Sharjah, United Arab Emirates

ARTICLE INFO

Article history:
Received 27 February 2020
Accepted 12 May 2021
Available online 27 May 2021

Keywords:
Finite element simulation
Flexural strengthening
Composite beams
Mechanical fasteners
Aluminum alloy plates
Mechanical behavior

ABSTRACT

This paper reports 3D nonlinear finite element (FE) models of reinforced concrete (RC) beams externally strengthened with mechanically fastened (MF) and externally bonded (EB) aluminum alloy (AA) plates. The measured and observed parameters of each specimen were obtained from an experiment conducted by the authors of this study. Each FE model adopted accurate material constitutive laws and appropriate element definitions to approximate the mechanical behavior observed during testing. A total of ten models were constructed based on the diameter, embedment depth, and arrangement of the expansion anchor bolt (EAB) as well as the presence or absence of epoxy. Results like the load-carrying capacity of the tested specimens as well as the failure modes like end-plate debonding (ED), local-plate debonding (LD), and plate rupture (PR) were accurately predicted. Additionally, Stress and strain contour plots were generated to investigate the FE models' mechanical behaviors. Finally, a parametric study was conducted to illustrate the effects of the flexural steel reinforcement ratio and AA plate grades on the models' structural response. It was concluded that the FE models could serve as a valid predictive platform for simulating the flexural behavior of RC beams strengthened with MF and EB AA plates.

1. Introduction

The incorporation of externally bonded reinforcement (EBR) in the form of composite sheets and plates has proven to be an effective approach in upgrading the capacity of reinforced concrete (RC) members [1-5]. Recent studies have focused on strengthening RC beams using externally bonded (EB) fiber-reinforced polymer (FRP) [6-8], aluminum alloy (AA) plates [9-15], and steel-wire mesh [16,17]. However, the anchorage techniques implemented in these EB composite systems suffer from drawbacks such as premature failures, skilled workmanship, cost, and time [18,19]. Therefore, researchers have adopted different anchorage techniques such as FRP wraps [13,20,21], FRP splay anchors [22], and mechanical fasteners [19,23-27] to mitigate these issues and prolong the member's loading life.

External strengthening using mechanical fastened FRP (MF-FRP) systems, in particular, has been a topic under scrutiny in recent years. The rigid mechanical interlock between the anchors and concrete holes induces an effective composite action between the structural member and composite material, thereby allowing the RC section to utilize a larger fraction of the composite's mechanical properties than a typical EB-FRP system. For instance, El Maaddawy and Soudki conducted a comparative study on implementing MF-FRP systems versus EB-FRP systems in flexurally strengthening of RC slabs using bonded and un-bonded FRP sheets [24]. The test results showed that the MF-FRP slab with bonded FRP sheets exhibited the largest strength gain and ductility when compared to the other strengthening schemes. Furthermore, the failure modes of all the MF-FRP slabs, with or without adhesives, were shifted from FRP delamination to concrete crushing, indicating a pure flexural failure. Thus, the existence of mechanical fasteners, despite the presence or absence of adhesives, restored the flexural behavior of the newly upgraded and strengthened RC slabs.

Although FRP composite sheets and plates serve as viable candidates in EBR applications, their susceptibility to brittle rupture failures and lack in ductility encouraged researchers to search for other novel composites that could overcome these drawbacks. In a recent study conducted by Rasheed et al. [13], high strength AA plates were used as EBR with FRP wraps EB at the ends of the plates

* Corresponding author.
E-mail address: rhaweeleh@aus.edu (R.A. Hawileh).

https://doi.org/10.1016/j.compstruc.2021.106573
0045-7949/

and at the ends and at the beams' mid-spans. The aim of this study was to investigate the viability of using AA plates in flexural strengthening applications. As a result, all of the strengthened RC beams achieved approximately the same strength gains as each other, whereas their ductility varied depending on the FRP-wrap configuration used. For instance, the specimens with FRP wraps at the plates' ends demonstrated approximately 80% of the ductility exhibited by the un-strengthened RC beam, whereas the specimen with FRP wraps at the ends and mid-span of the plates have superseded that of the un-strengthened RC beam. Unfortunately, premature failure modes were reported for all the strengthened FRP wrapped specimens such that local-plate debonding (LD) failures were observed. This indicated that the implementation of AA plates, with a more effective anchorage system, would mitigate any type of debonding and allow the AA plated RC sections to resist larger deformations.

In previous studies [26,27], the authors of this study have investigated the effects of using mechanically fastened (MF) and externally bonded (EB) AA plates on the flexural strength, stiffness, and ductility of RC beams. A total of sixteen flexure-deficient RC beams were prepared where fifteen of these specimens were strengthened using AA plates, and varied based on the type of anchorage system used. Mainly, these variations were centered on the spacing and layout of mechanical fasteners while alternating the usage of an adhesive on the plated region. As a result, almost 86% of the beams that were MF and/or EB with AA plates failed by plate rupture (PR); indicating that the specimens fully utilized the mechanical properties of the AA plates. In addition, the authors have reported the ductility gain associated with the delay in premature failure and concluded that using MF at the plates' ends corresponded to the most optimum MF layout for both strength enhancement and ductility.

Over the recent years, finite element (FE) modeling has aided researchers and civil engineers in studying the nonlinear response of externally strengthened RC members using FRP composites [28-30]. Its accuracy and precision helped numerically simulate the flexural behavior of FRP-strengthened members by verifying predictions like maximum attained loads, deflections at ultimate loads, load–deflection response plots, and failure modes against those of the experiment [30]. These validated FE models could then be used to study the stress and strain propagations throughout the models during all stages of loading without the expense of physically measuring them during a test. In addition, some researchers take advantage of the FE environment to perform parametric studies and identify the effect of each parameter on the response of the model by illustrating these conclusions via graphical representations (i.e., contour plots).

Furthermore, experimental data obtained from published articles were used to develop FE models that simulate RC beams strengthened with AA plates, and study the effect of different plating schemes and mechanical properties on the response of each retrofitted mode [14,15]. This motivated the authors of this study to develop FE models of MF AA plated (MF-AAP) specimens collected from a recent experimental investigation [26,27]. In addition, scarce published articles related to FE modeling of MF composite systems in strengthened RC members exist in the literature [31,32]. Therefore, the authors of this paper attempt to reinforce this gap in the literature, and develop FE models simulating the flexural behavior of MF-AAP specimens tested in a previous study using the commercial FE software, ANSYS 19 [33].

The objective of the present study is to utilize three-dimensional nonlinear FE modeling to predict the flexural behavior of RC beams that were externally strengthened using expansion anchor bolts (EAB) with bonded or un-bonded AA plates, and simulate the fracturing behavior of the AA plates in each strengthened specimen. The geometric and mechanical properties of the FE models were collected from a previous experimental study conducted by the authors of this paper [26,27]. The developed FE models employed constitutive material laws that simulate concrete in compression and tension, steel yielding, AA plate yielding and rupture, and adhesive delamination between the AA plate and concrete soffit. FE model validation was carried out by comparing predictions like the maximum attained loads, deflection at ultimate load, load–deflection response plots, load–strain response plots, and failure modes of each model to those observed in the experiment. A brief overview of the model behavior was covered by generating stress and strain contour plots for the elements in selected FE model. Based on the good agreement between the predictions and experiment, an extensive parametric study was carried out to investigate the effect of increasing the bottom steel reinforcement diameters and AA plate grades on the structural response of the models. To the authors' top knowledge, the literature is lacking adequate information on the effect of the steel reinforcement ratio and AA plate grades on the flexural performance of strengthened RC beams with AA plates. Accordingly, the outcomes of the parametric study conducted in this paper would enable researchers/engineers to understand the underlying relationships between both the bottom steel ratio and AA plate grades, respectively, with their structural response.

2. Summary of experimental program

The FE model development reported herein was based on an experimental investigation conducted by the authors of this paper [26,27]. The evaluated flexural response of RC beams strengthened with mechanical fasteners and bonded/un-bonded AA plates were collected for FE model verification purposes. All the tested specimens were subjected to a monotonically increasing four point bending up until failure of the specimens was evident through physical and measured observations. The RC beams were designed to fail in flexure as per the international design codes and standards, ACI 318–19 guidelines [34]. The test matrix consisted of sixteen RC beams, where one RC beam was left un-strengthened to serve as the control beam, one RC beam was EB with an AA plate, and the remaining fourteen RC beams were externally strengthened with MF with or without EB AA plates. Each RC beam member consisted of 125 mm $\times$ 240 mm $\times$ 1840 mm in width, length and height, respectively. The flexural reinforcement consisted of two ϕ 10 mm bars in the bottom (area = 157 mm^2) and two ϕ8 mm bars in the top (area = 100.48 mm^2), and the shear reinforcement consisted of ϕ8 mm vertical stirrups spaced at 100 mm center-to-center. Fig. 1 shows the dimensions, reinforcement details, and loading schemes for each tested specimen [26] Table 1.

The externally strengthened RC specimens were varied based on the diameter, embedment depth, and spacing of the mechanical fasteners while alternating the application of adhesive bonding. During strengthening, the mechanical fasteners and adhesive used were expansion anchor bolts (EAB) and epoxy, respectively. Two types of EAB were used: HST3-M10 and HST3-M12, where they varied based on the size of the diameter and embedment depth. A brief outline of the test matrix is presented in Error! Reference source not found. in which the varying parameters like the type of anchorage, EAB details, and EAB layout are simplified in the schematics shown in Fig. 2. The prefixes "B", "BE", "M10L", "M10H", "M12L", "M12H", "M10E", and "M12E" in the specimen designation refer to "beam without epoxy", "beam with epoxy", "low number of HST3-M10 EAB", "high number of HST3-M10 EAB", "low number of HST3-M12 EAB", "high number of HST3-M12 EAB", "HST3-M10 EAB on the edges", and "HST3-M12 EAB on the edges", respectively. For example, BEM10H refers to a beam strengthened with AA plates using epoxy and a high number of HST3-M10 EAB. It

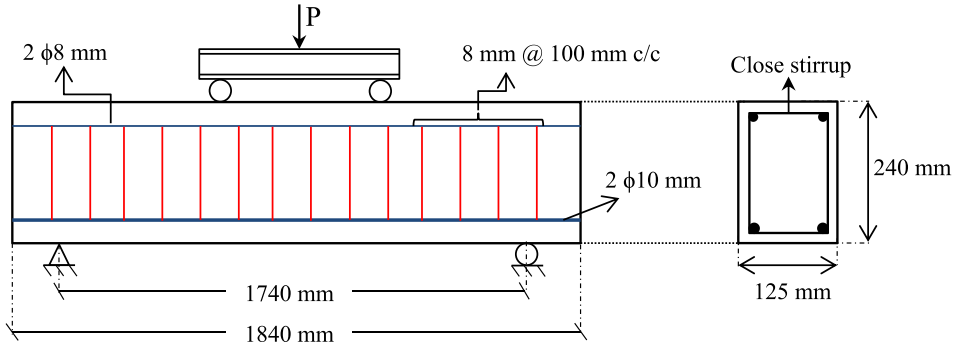

Fig. 1. RC beam details and load setup [27].

Table 1
Test matrix and FE model designation [27].

Specimen Designation	FE Model Designation	Anchorage		EAB details			EAB layout	
		Epoxy	EAB	Spacing (mm)	Diameter (mm)	Embedment Depth (mm)	Series	Edge
CB	CB-FE	–	–	–	–	–	–	–
CBE	CBE-FE	√	–	–	–	–	–	–
BEM10H	BEM10H-FE	√	√	100	10	65	√	–
BEM10L	BEM10L-FE	√	√	200	10	65	√	–
BEM12H	BEM12H-FE	√	√	100	12	80	√	–
BEM12L	BEM12L-FE	√	√	200	12	80	√	–
BM10H	BM10H-FE	–	√	100	10	65	√	–
BM12H	BM12H-FE	–	√	100	12	80	√	–
BEM10E	BEM10E-FE	√	√	100	10	65	–	√
BEM12E	BEM12E-FE	√	√	100	12	80	–	√

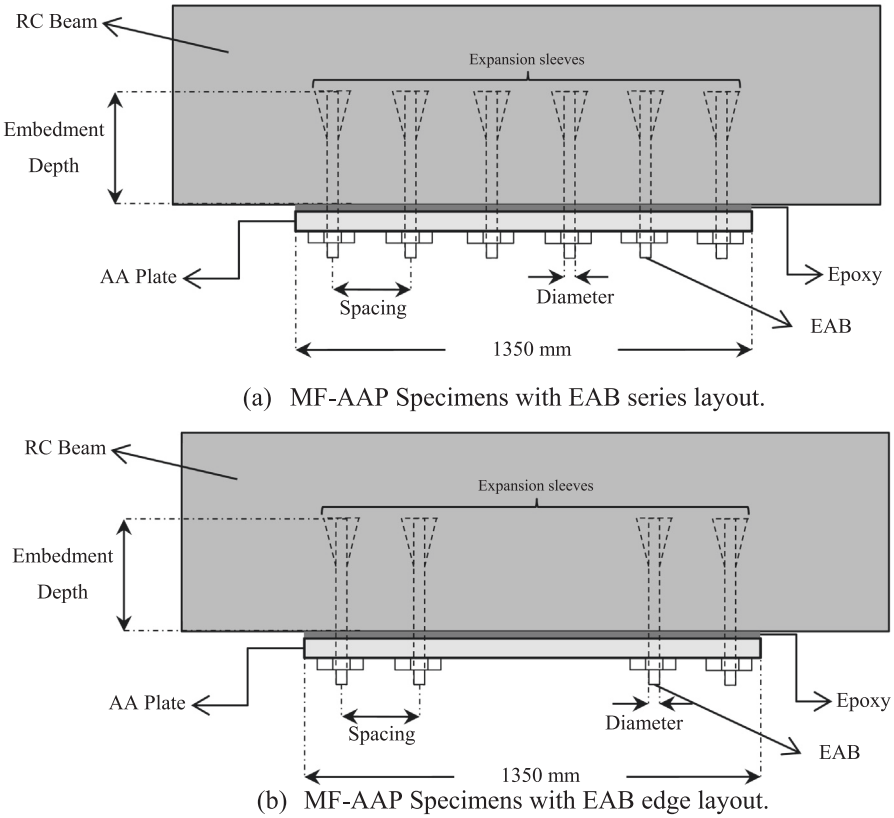

Fig. 2. MF-AAP specimen details [27].

Table 2
EAB mechanical and geometric properties [27].

EAB Details[a]	HST3 M10 × 90	HST3 M12 × 105
f_{uta} (MPa)	800	800
$A_{se,V}$ (mm^2)	58	84.3
d_o (mm)	10	12

[a] : f_{uta}: tensile strength; $A_{se,V}$ = area of EAB sleeve; d_o = diameter of EAB.

is worth mentioning that the experimental program consisted of replicas for all of the specimens except CB, CBE, BEM10E, and BEM12E. A detailed overview of the experimental program and test parameters is reported in [26].

Fig. 2 shows the different anchorage approaches adopted during the strengthening preparations in [26], where Fig. 2**(a)** describes specimens BEM10L/H and BEM12L/H, and Fig. 2**(b)** describes specimens BEM10E and BEM12E. The EAB consist of expansion sleeves at their ends to promote rigid interlocks between the EAB and inner concrete aggregates. This mechanism prevents premature failures like EAB-pullout or EAB-pryout and was accounted for during the model development. Table 2 presents the EAB mechanical and geometric properties that were used during this study. It is worth mentioning that the installation of bolts was conducted such that the bolts did not interfere with the internal steel reinforcement to prevent galvanic corrosion [26,27].

3. FE model description

This section describes the element definition, material properties, and modeling techniques followed herein. Fig. 3**(a)** shows the side view of a typical developed FE model, where two planes of symmetry where identified; at the mid-span of the model and at the center of the cross section, as shown in Fig. 3**(b)**. Restraining at both planes of symmetry reduces the number of elements and equations needed to converge to the solution, which greatly simplifies the computation and significantly reduces the analysis time [28].

3.1. Element definitions

The elements for each tested specimen were defined separately using the FE element database stored inside the ANSYS environment [33]. Each element was selected based on the mechanical characteristics exhibited by the material during testing. For instance, concrete was modeled using SOLID65 elements, since it crushes in compression and cracks in tension [33]. The SOLID65 elements also have the capabilities of visually demonstrating the cracking-patterns at each load-step [33]. The internal steel reinforcing bars were all treated as truss elements that resist compressive and tensile stresses. Therefore, LINK180 3D spar elements were used to capture this uniaxial compression-tension behavior [33]. The AA plate, loading and supporting plates, and EAB were modeled using SOLID185 elements [33], since similar techniques were observed in other studies involving RC beams strengthened with AA plates [11,14]. Finally, epoxy was modeled using INTER205 elements to help simulate the delamination between the AA plate and concrete surface during the load steps [33]. Several published FE-related articles have successfully implemented delamination simulations using INTER205 elements [11,14,15]. The MF-AAP specimens with un-bonded AA plates, BM10H and BM12H, were modeled using TARGE170 and CONTA174 elements [33]. The CONTA174 elements are responsible for simulating both contact and sliding interactions between the TARGE170 elements [33]. This target-contact interface was defined using a pair-base contact argument in which both elements were assumed to behave

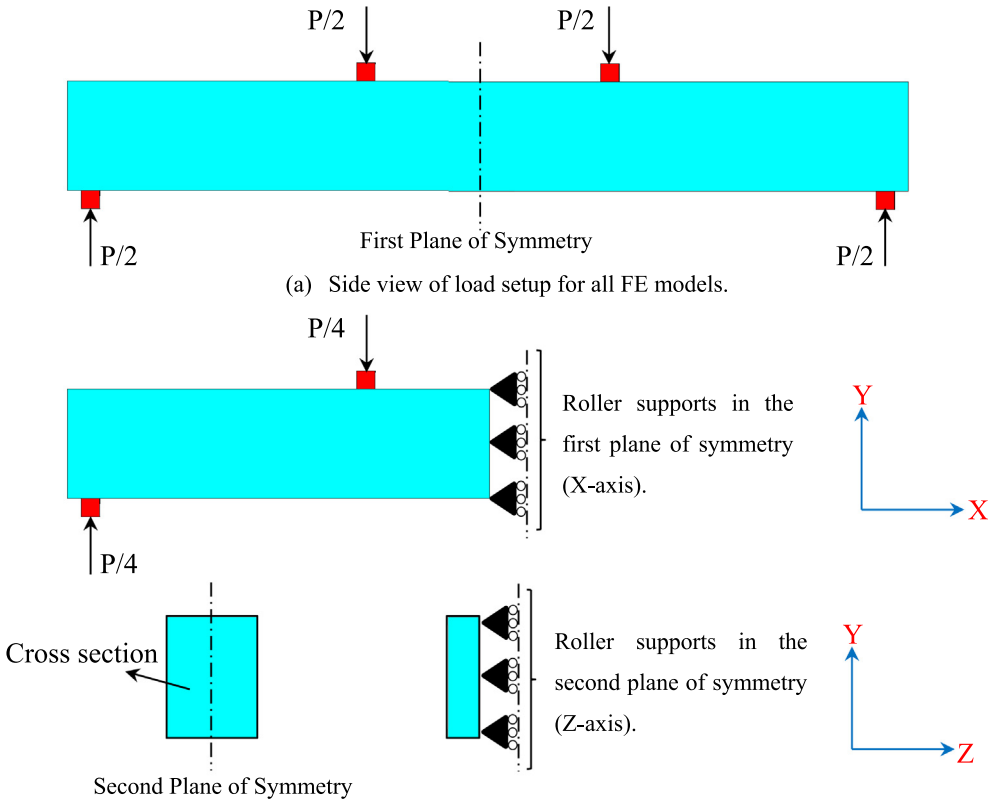

(a) Side view of load setup for all FE models.

(b) Restrained model in the longitudinal and transverse directions (X-direction and Z-

Fig. 3. Typical FE model schematic.

in a flexbile-flexible interaction with a coefficient of friction value of 0.3 [33].

3.2. Material constitutive laws

The material properties employed within the elements assisted the FE models in exhibiting their nonlinear behavior during loading. Idealized stress–strain curves obtained from unique constitutive laws were used when defining the material properties. Fig. 4 shows the idealized stress–strain curves employed for the concrete elements, where Fig. 4**(a)** defines the concrete in compression and Fig. 4**(b)** represents the concrete during tension. The concrete compressive response curve was modeled using the following relationship developed by Hognestad et al. [35]:

$$f_c = \begin{cases} f'_{cc} \cdot \left[\frac{2\cdot\varepsilon_c}{\varepsilon_{co}} - \left(\frac{\varepsilon_c}{\varepsilon_{co}}\right)^2\right], for \quad 0 \leqslant \varepsilon_c \leqslant \varepsilon_{co} \\ f'_{cc} - \frac{0.15 f'_{cc}}{(\varepsilon_{cu}-\varepsilon_{co})} \cdot (\varepsilon_c - \varepsilon_{co}), for \quad \varepsilon_{co} \leqslant \varepsilon_c \leqslant \varepsilon_{cu} \end{cases} \quad (1)$$

where f_c = concrete compressive stress, f'_{cc} = concrete cylinder compressive strength taken as 36 MPa [26], ε_c = concrete strain, ε_{co} = concrete strain corresponding to f'_{cc} $\left(\varepsilon_{co} = \frac{2f'_{cc}}{E_c}\right)$, ε_{cu} = strain at concrete crushing taken as 0.0038, and E_c = Young's modulus of elasticity taken as $E_c = 4700\sqrt{f'_{cc}}$ [34]. The concrete Poisson's ratio was assumed to be v_s = 0.2. Furthermore, the concrete tensile response was modeled using an elastic linear line up to tensile rupture of $f_t = 0.62\sqrt{f'_{cc}}$ [36]. Afterwards, the tensile strength exhibited a 40% drop in capacity ($0.6f_t$) followed by an inversely linear line that reaches a tensile stress of 0 MPa at $6\varepsilon_t$, where ε_t is the concrete tensile strain corresponding to f_t.

The yield strength values of the internal steel reinforcement for both the longitudinal and transverse steel bars were reported as 550 MPa [26]. These values were used in the stress–strain response curves of steel by assuming a perfectly elastic plastic behavior. Several numerical studies involving FE model development of retrofitted RC members have used this assumption [11,28,29]. Moreover, the Young's modulus of elasticity was input as E_s = 200 GPa and the Poisson's ratio was input as v_s = 0.3. Since some of the MF-AAP specimens failed in plate rupture (PR), the stress–strain response of the AA plates was modeled using a bi-linear relationship. Fig. 5 presents the idealized stress–strain curve that was input for the AA plate elements, where the curve starts with a linear elastic increase up to the measured yield strength, 150 MPa [26], followed by another linear increase up to the measured ultimate tensile strength, 300 MPa [26]. This assumption will help capture the load step corresponding to PF failure; indicating whether the FE model simulated the fracturing behavior of the tested specimen. The Young's modulus of elasticity and Poisson's ratio of the AA plate elements were input as E_s = 70 GPa and v_s = 0.33 [26].

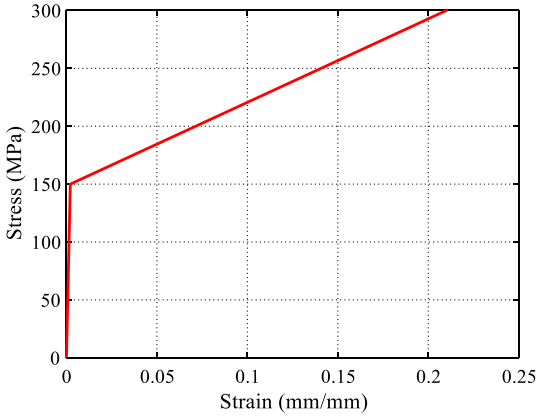

Fig. 5. Bi-linear stress–strain curve of AA plate.

The epoxy adhesive's mechanical properties were reported as 80 MPa, 40 MPa, 8000 MPa, 4000 MPa and 30 MPa for the compressive strength, flexural strength, modulus of elasticity under compression, modulus of elasticity in flexural, and tensile strength [26]. Furthermore, the process of delamination was simulated using a bond stress-slip model that accounts for the mechanical and geometric properties of the concrete, steel reinforcement, and composite material used during the test. In this paper, the bond-slip model developed by Lu et al. [37], shown in equation (2), was adopted to generate the curve shown in Fig. 6. The model assumes an increasing segment up to an ultimate shear stress (τ_{max}) corresponding to a slip (s_o), followed by an exponential decay until the failure slip (s_f). The failure slip was assumed to equal four times s_o($4s_o$), similar to previous studies [30,31,38]. The bond-slip parameters τ_{max} and s_o were evaluated using Equations (3) – (7) proposed by Lu et al. [37].

$$\tau = \begin{cases} \tau_{\max} \cdot \sqrt{\frac{s}{s_o}}, for \quad s \leqslant s_o \\ \tau_{\max} \cdot e^{-\alpha\left(\frac{s}{s_o}-1\right)}, for \quad s > s_o \end{cases} \quad (2)$$

where

$$\tau_{\max} = 1.5 \cdot \beta \cdot f_t \quad (3)$$

$$s_o = 0.0195 \cdot {\beta_w}^2 \cdot f_t \quad (4)$$

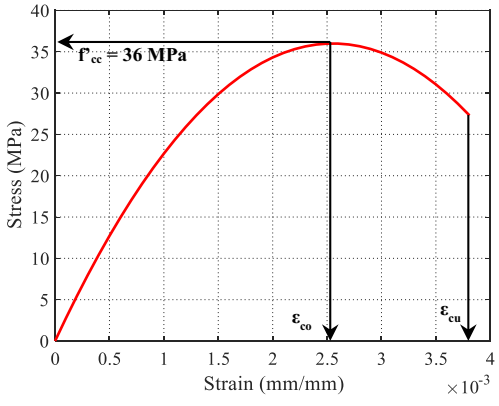

(a) Compressive stress-strain curve.

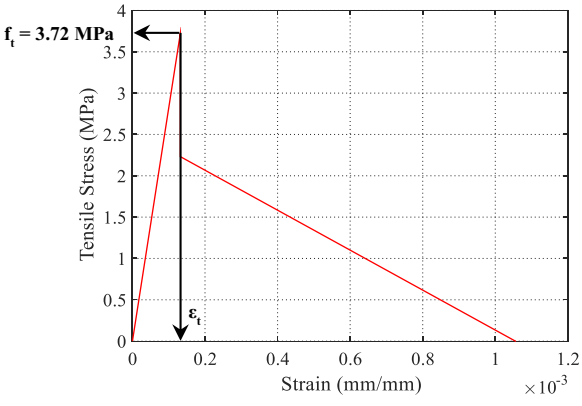

(b) Tensile stress-strain curve.

Fig. 4. Idealized stress–strain curves employed for the concrete elements.

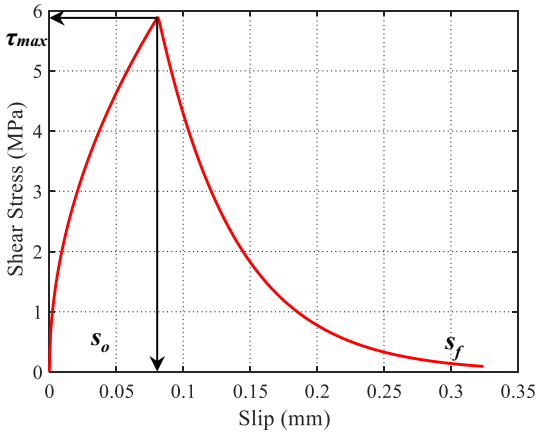

Fig. 6. Shear stress-slip model for INTER205 elements.

$$\alpha = \frac{1}{\frac{G_f}{\tau_{max} s_o} - \frac{2}{3}} \tag{5}$$

$$G_f = 0.308 \cdot \beta_w^2 \cdot f_t \tag{6}$$

$$\beta_w = \sqrt{\frac{2.25 - \frac{b_f}{b_c}}{1.25 + \frac{b_f}{b_c}}} \tag{7}$$

where s = slip between the concrete soffit and AA plate, β_w =-width ratio factor, α = factor depends on interfacial rupture energy, bond strength, and slip at peak, G_f = interfacial rupture energy, b_f =-width of AA plate, and b_c = width of concrete section.

3.3. Modeling techniques

All elements were discretized such that the nodes between each unique element coincide with each another. This granted ideal load transfer across the nodes and greatly reduced computation complexity. The specimens that were EB with AA plates were meshed using the cohesive zone material (CZM) model. The CZM model is a function of the traction and the slip between the strengthening material and its host, such that the bond stress-slip curve generated in the previous section was incorporated to induce fracture mechanisms within the INTER205 elements. The thickness of epoxy was assumed to equal 1 mm, similar to previous studies.

Furthermore, the volume of EAB in the models that were MF with bonded/un-bonded AA plates were assumed to be uniform cylinders, where the expansion sleeve part was merged with the surface of the concrete. This simulated the rigid interlock between the EAB and concrete. Moreover, the 3 mm segment of the EAB that goes through the AA plate was also merged to the plate elements to simulate the bolting mechanism. The symmetry planes in the longitudinal and transverse directions were situated at the center of the EAB direction. Therefore, the EAB at mid-span of the models were constructed as quarter cylinders and the EAB away from the mid-span of the models were constructed as semi-cylinders, as shown in Fig. 7.

The contact between the AA plate and concrete surface in specimens BM10H and BM12H was modeled using contact-target elements, as shown in Fig. 8. This was assumed throughout the entire plate such that the shear strength induced by the friction between the surfaces of the AA plate and concrete were accounted for during the analysis. On the other hand, the contact between the AA plate and concrete in the MF specimens with bonded AA plates was modeled using INTER205 elements, where the INTER205 elements were not modeled throughout the length of the plate. This

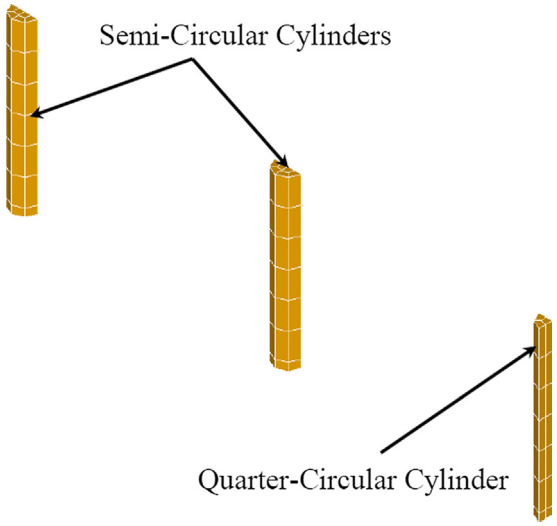

Fig. 7. EAB elements for MF-AAP specimens.

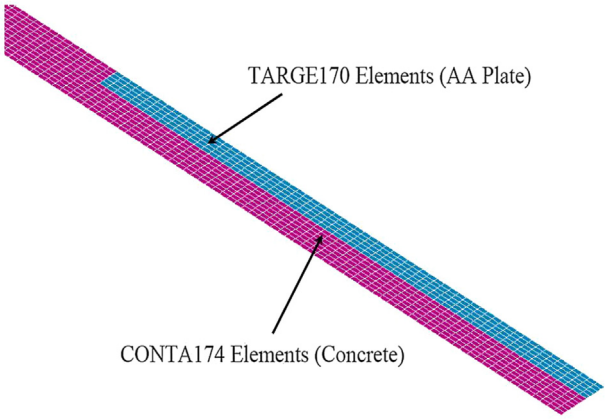

Fig. 8. CONTA174 and TARGE170 element assignments.

is because the CZM command is unable to be executed when there are elements other than the INTER205 elements. Therefore, a 20 mm horizontal gap was left such that the EAB were able to be merged within the concrete and AA plate while not interfering with the CZM command assigned within the INTER205 shell elements, as shown in Fig. 9, where Fig. 9(a) shows the FE models of specimens MF across the AA plates and Fig. 9(b) shows the FE models of the specimens MF at the edges of the AA plates.

3.4. Convergence criterion

During displacement controlled loading, ANSYS automatically treats each user–defined displacement as a unit–step to evaluate the nodal stresses and strains within the element. The numerical solver used to help the model achieve convergence was the Newton–Raphson method where, the solver iteratively reduces the time-step (displacement) until a solution is found. Afterwards, it iterates to the next step such that the numerical solver begins evaluating the problem until convergence is achieved. However, ANSYS requires a user-defined convergence tolerance to abide by. Typically, this value would range between 0.05 and 0.2 [11]. Therefore, in this study, the force convergence tolerance limit value was taken as 0.1.

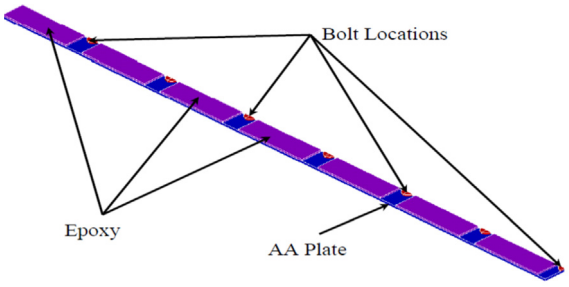

(a) Epoxy for specimens BEM10H/L and BEM12H/L.

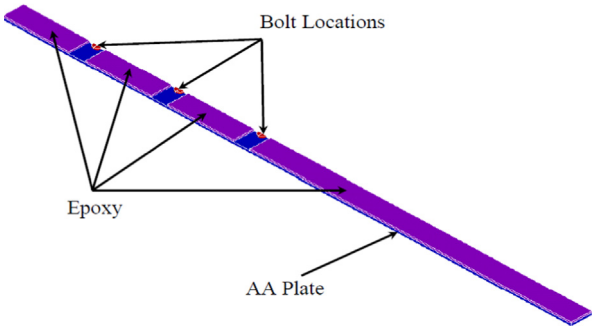

(b) Epoxy for specimens BEM10E and BEM12E.

Fig. 9. Contact simulation for MF-AAP specimens with epoxy.

3.5. Failure criteria

The analysis of each model was stopped based on the type of failure exhibited. In this study, the failure modes demonstrated during testing were: concrete crushing (CC), plate rupture (PR), end-debonding (ED), and intermediate-crack debonding (IC). These failure modes can be numerically distinguished by monitoring the stress and strain propagation of each element. During the tests, all of the beams exhibited crushing prior to their unique failure modes. This helped define a criterion for which the analysis should terminate until crushing and one of the three latter imposed failure modes. These failure modes were defined as:

1. Flexural failure (FF), which is when steel yielding occurs followed by concrete crushing. Crushing of concrete was defined once the third principal strain in the top compression elements at mid-span of the FE model exceeds −0.003 (negative and positive signs indicate compressive and tensile stresses/strains).
2. Plate rupture (PR), which is defined when the first principal strain of the AA plate exceeds + 0.22, which is the ultimate strain of the AA plate during the experiment conducted by authors of this study [26,27]. It is worth mentioning that steel yielding followed by concrete crushing also occurred for specimens that were MF.
3. End-plate debonding (EPD), which is defined as the shear stress at the ends of the plates that exceeds 5.90 MPa, as per τ_{max} demonstrated in Fig. 6. This particular failure mode occurred for the specimen that was EB with an AA plate prior to EPD, where steel yielding followed by concrete crushing occurred.

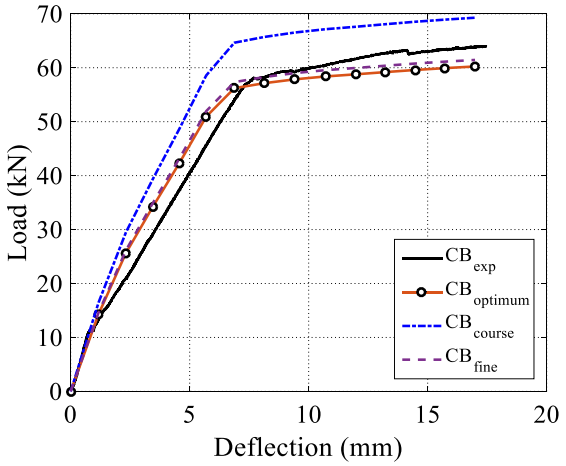

Fig. 10. Mesh sensitivity analysis for model CB-FE.

4. Local-plate debonding (LPD), which is similar to failure criteria (3) but at mid-span of the plate. Similarly, steel yielding followed by concrete crushing was demonstrated prior to LPD.

The models that exhibited failure modes (3) and (4) were not fully analyzed due to rigid body motion of the plate. This poses a programmatic problem for ANSYS in which insufficient number of constraints is unable to prevent rigid body motion. Therefore, the results of these models were extracted at the final load increment, before terminating the analysis.

4. Results and discussion

4.1. Mesh sensitivity analysis

The FE model's discretization was carried out by constructing three models simulating specimen CB (CB-FE) with different element mesh sizes. These models were designated CB_{course}, CB_{fine}, and $CB_{optimum}$ in which each model was analyzed during a certain time period, to obtain an efficient model in terms of both accuracy and computation expense. Table 3 shows the three models that were used during this approach, where the mesh size of each element, number of concrete elements, and time of analysis was tabulated. It is worth mentioning that the mesh size selection was based on nodal intersections throughout each model such that ideal stress transfer is induced between the elements. The number of concrete elements were demonstrated to understand the size of the problem being solved. As a result, CB_{course} took the least time, 1749 sec, due to the least number of equations (elements) solved, whereas CB_{fine} took the longest time, 3835 sec. The accuracy was assessed by plotting load versus mid-span deflection curves of the three models against that of the tested specimen (CB), as shown in Fig. 10. It was observed that the curve in model CB_{course} strongly deviated away from that of specimen CB, while models CB_{fine} and $CB_{optimum}$ have demonstrated negligible difference. Therefore, $CB_{optimum}$ was selected as the final model since it contains a lower number of equations than that of CB_{fine} and a better correlation than that of CB_{course}.

Table 3
Number and size of concrete elements during analysis.

No.	Model Designation	Mesh Size (mm × mm × mm)	Number of Concrete Elements	Computation Time (sec)
1	CB_{course}	20 × 20 × 20	1656	1749
2	CB_{fine}	10 × 5 × 5	52,992	3835
3	$CB_{optimum}$	10 × 10 × 5	26,496	2443

4.2. Model validation

The predictions made in each model were extracted and compared to the measurements taken during the test. This step was to ensure the model is simulating the nonlinear behavior of the tested specimens to present practical strain and stress contour plots along the models, without physically measuring them. In addition, model validation assisted the authors of this paper in taking a step forward and performing parametric studies that could serve as a guide for structural engineers in design situations. Details regarding this approach will be covered in the following sections.

4.2.1. Failure modes and cracking patterns

The tested specimens all failed by crushing of concrete and yielding of steel [26,27]. However, plate rupture (PR), end-plate debonding (EPD), and local-plate debonding (LPD) were observed for different anchorage systems. For example, specimen CBE demonstrated EPD followed by a drop in its loading capacity at low deflections, whereas specimens BEM10E and BEM12E demonstrated LPD after resisting significant deflections during the test. The remaining specimens that consisted of linear EAB layout failed in PF at the location of the EAB. Clear flexural cracks were observed for all of the specimens except specimen CBE due to premature failure at a lower deformation. Model CB-FE was able to exhibit flexural crack and concrete crushing similar to that of specimen CB, as shown in Fig. 11**(a)**, and models CBE-FE, BEM10E-FE, and BEM12E-FE were able to simulate the nonlinear failure modes like EPD and LPD, as shown in Fig. 11**(b)–(d)**. These failure modes involved rigid body motion; thus, the models were unable to continue analyzing and viewed the scaled full distance traveled by the plate (i.e. the solution diverged). The predictions made by these models were extracted at the final load step, where this served as the first step in validating the predictions in the following

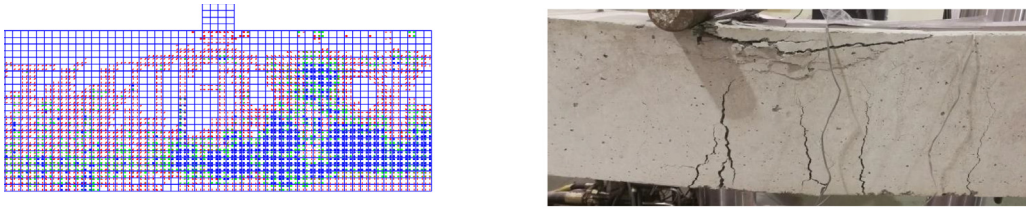

(a) Comparison between CB-FE and CB.

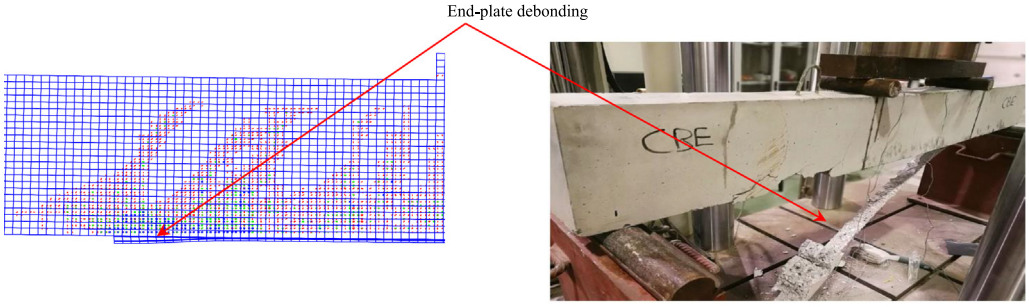

(b) Comparison between CBE-FE and CBE.

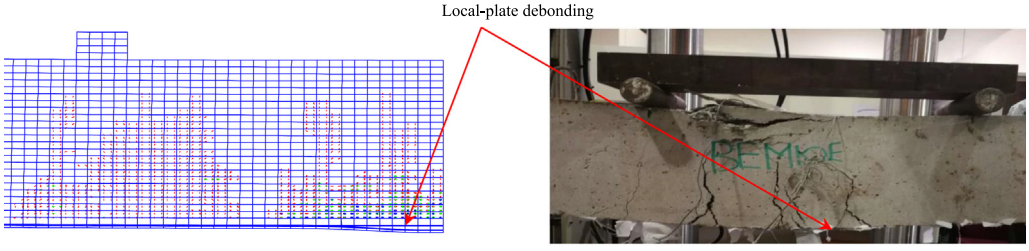

(c) Comparison between BEM10E-FE and BEM10E.

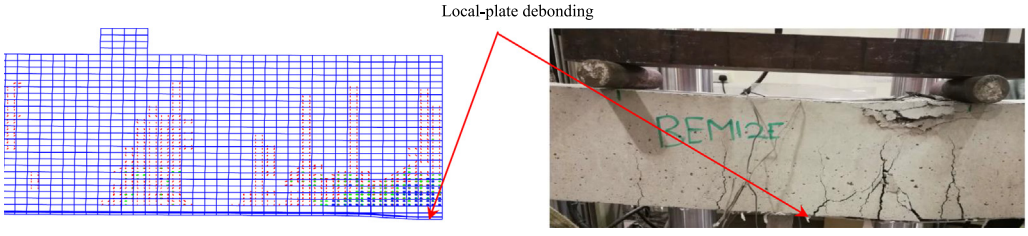

(d) Comparison between BEM12E-FE and BEM12E.

Fig. 11. Failure modes and cracking patterns of selected specimens and models.

sections. It is worth mentioning that the specimens that consisted of a linear EAB layout were verified in terms of strain predictions discussed in the following section.

4.2.2. Load-strain response curves

Fig. 12 shows the load–strain response plots obtained from the FE models and tested specimens. It can be observed that good agreement exists between the predicted and experimental curves. Moreover, all of the models numerically simulated concrete crushing and steel yielding at peak loads. Models BM10H-FE, BM12H-FE, BEM10H-FE, BEM12H-FE, BEM10L-FE, and BEM12L-FE have numerically predicted AA plate rupture at strain predictions of 0.22. Therefore, other predictions made by these models were extracted until the load step where AA plate rupture was evident. This is not observed during the test since the strain gauges malfunctioned slightly after plate yielding due to excessive deformation in both the plate and strain gauge instruments [26]. It is worth mentioning that the scale of the plots was maintained between −0.005–+0.015 such that the large strain predictions in the AA plate do not hide the concrete and steel strain curves in the Fig. 12.

Furthermore, the MF-FE models were capable of predicting larger aluminum strain values than model CBE-FE, indicating larger deformations and increased curvature. The increased curvature allows the sections to resist larger tensile and compressive stresses in the longitudinal steel reinforcement and top concrete compression fibers. These MF models exhibited larger strength and ductility, as shown in Fig. 12**(b)–(j)**.

4.2.3. Load-deflection response curves

Fig. 13 shows the load versus mid-span deflection curves of the models analyzed with respect to the tested specimens in [26]. It is clearly indicated that good agreement exists between the predicted and experimental load versus mid-span deflection curves. These curves were generated up until the program terminated, due to EPD/LPD of the plate, or until PF as shown Fig. 12**(b)–(h)**. This comparison provided a final verification of the models such that they were able to simulate the non-linear load–deflection

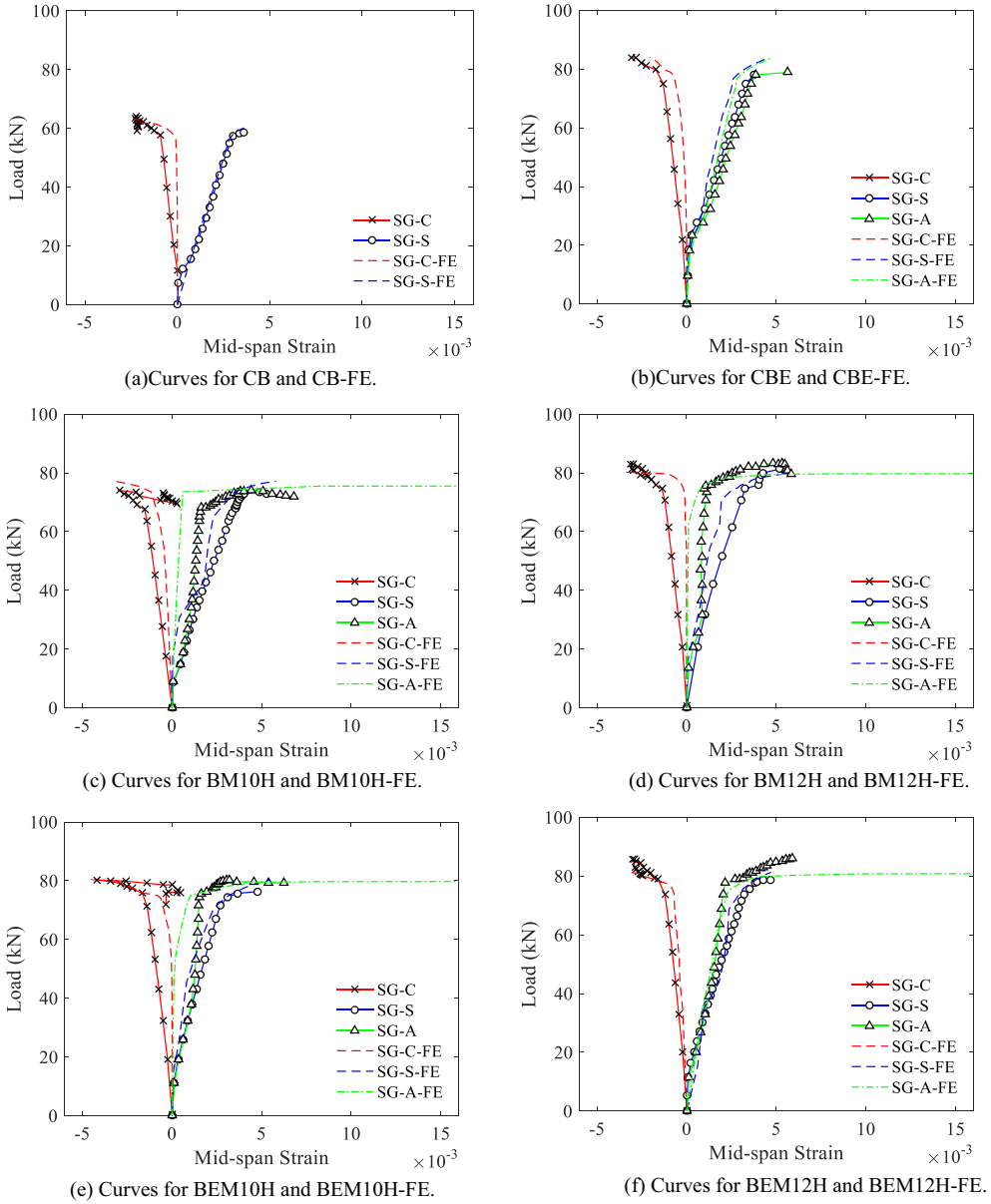

(a)Curves for CB and CB-FE. (b)Curves for CBE and CBE-FE.

(c) Curves for BM10H and BM10H-FE. (d) Curves for BM12H and BM12H-FE.

(e) Curves for BEM10H and BEM10H-FE. (f) Curves for BEM12H and BEM12H-FE.

Fig. 12. Load versus mid-span strain between FE models and tested specimens.

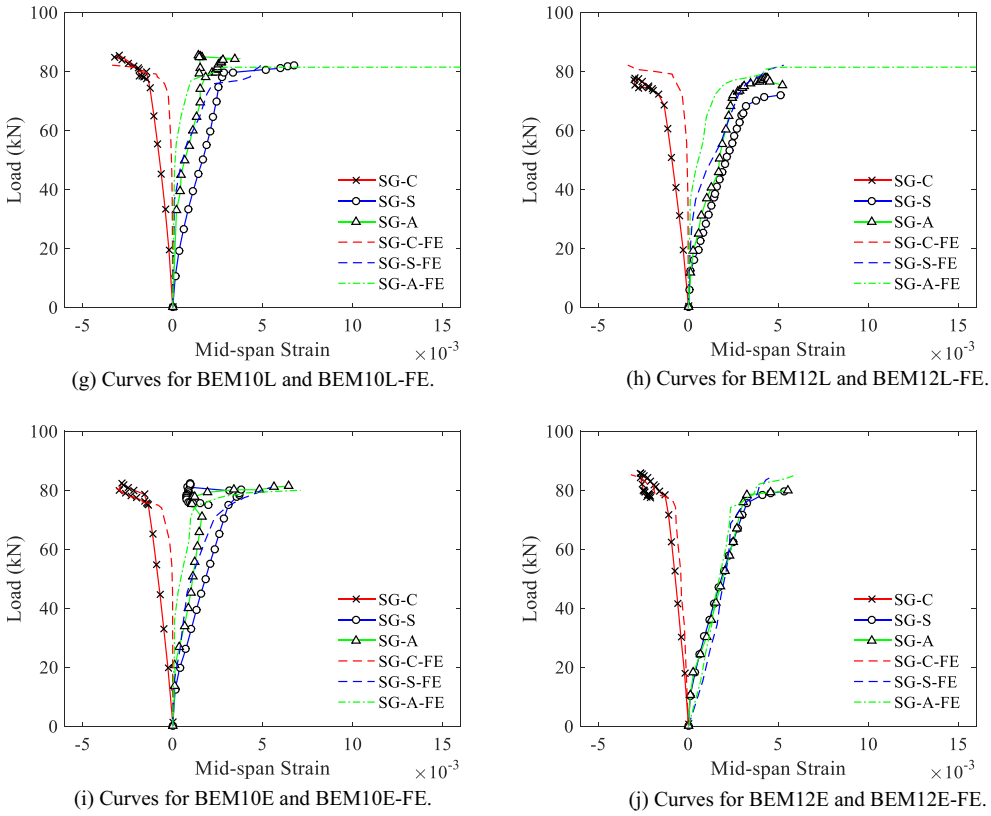

(g) Curves for BEM10L and BEM10L-FE. (h) Curves for BEM12L and BEM12L-FE.

(i) Curves for BEM10E and BEM10E-FE. (j) Curves for BEM12E and BEM12E-FE.

Fig. 12 (*continued*)

response demonstrated by the strengthened specimens during testing. The FE models were successful in predicting the strength gain achieved in specimens that were strengthened using AA plates without any significant reduction in ductility.

The presence of EAB in both the models and tested specimens helped in exhibiting larger ductility than those that were strengthened using only EB AA plates without EAB (CBE and CBE-FE). It was observed that larger sized EAB increased the ultimate load-carrying capacity of BM12H-FE when compared to BM10H-FE, as shown in Fig. 13**(b)**, where BM12H-FE behaved similar to the models that were strengthened using MF and EB AA plates. Therefore, using larger EAB without any epoxy had the same strength gain as those strengthened with MF and EB AA plates.

Furthermore, the EAB layout influenced the ductility of the models where using EAB as end-anchors allowed the section to utilize a larger segment of the AA plate when compared to the linear EAB layout. By using larger EAB at the ends of the plates, BEM12E-FE demonstrated the most efficient load versus deflection curves whereby both the strength and ductility exceed that of the unstrengthened specimen. These findings can guide retrofit engineers in the design for supplementing flexural members with both strength and ductility gains. It is worth mentioning that the initial stiffness exhibited by the FE models relative to that of the tested specimens was due to the plate slip that would occur in the experiment. As a result, the load–displacement curve would soften at a higher rate than those of the model.

4.2.4. Summary and comparison of results

Table 4 presents a brief summary of the predicted and experimental results. It was observed that all FE models were able to predict the peak load and corresponding deflection with absolute percentage errors less than 7%. Model CB-FE recorded a maximum deviation of 6.23% in peak load prediction from that of the experiment, whereas model BEM10E-FE recorded a maximum deviation of 6.71% in deflection at peak load from that of the experiment. Moreover, all FE models were successful in capturing the failure modes observed from the specimens during testing. By implementing this robust model validation approach, the authors of this paper can trust these models such that the model behavior, in terms of stress and strain propagations throughout the model, could be studied while conducting an extensive parametric study on the different properties of an AA-strengthened RC member.

5. Model behavior

5.1. Plate contribution

Fig. 14 shows the first principal strain contour plots along the plates' directions for models BEM12H-FE, BEM12L-FE, and BEM12E-FE. These models were selected to investigate the effect of the EAB layout used on the strain distribution in the plates. It was observed that models BEM12H-FE and BEM12L-FE demonstrated PF failures at mid-span of the beam perpendicular to the bolt, as shown in Fig. 14**(a) and (b)**, by reaching the previously imposed ultimate strain value of 0.22. In addition, strain concentrations were located at the EAB within the vicinity of the loading plates, which indicated poor contribution of the entire plate length at peak load. This also affected the ductility of the specimens since a relatively small plate length was resisting the bending stresses; leading to PF. However, model BEM12E-FE mitigated these drawbacks by utilizing the un-anchored length of the AA plate within the vicinity of the loading plates. Thus, demonstrating strain distribution along a larger length of the plate, as shown in Fig. 14**(c)**. It is worth mentioning that LPD occurred before PF, therefore, the plate did not initiate any fracturing behavior. Larger plate contribution

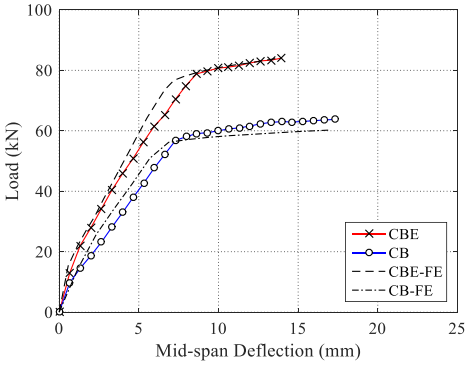

(a) Specimens CB and CBE.

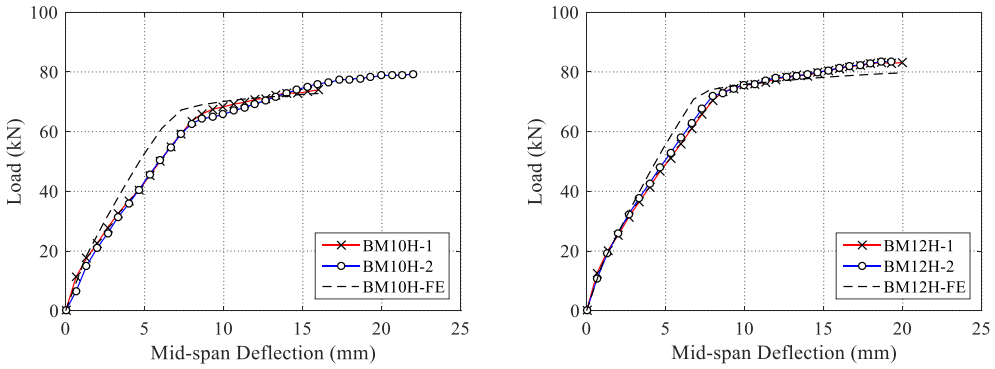

(b) Specimens BM10H and BM12H.

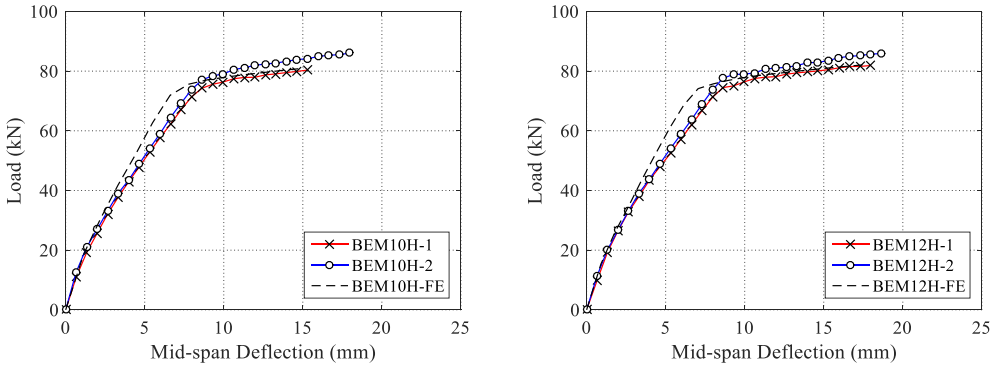

(c) Specimens BEM10H and BEM12H.

Fig. 13. Load versus mid-span deflection curves for FE models versus tested specimens.

indicated more strain distribution thereby allowing the beam to resist larger deformations and demonstrated significant ductility gains compared to the other models.

5.2. Local behavior

The local behavior of the anchors was also investigated in the context of strain distribution in both × and y directions as well as the concrete crack within their vicinity. For brevity, model BEM12E-FE was selected since it exhibited substantial strength gains and ductility during testing [26,27]. Fig. 15 shows the strain contour plots in the × (longitudinal) and y (vertical) directions. It can be observed that the anchors experience greater strain magnitudes in the bottom more than the top, which is expected since the AA plate is situated in the bottom region of the anchors. Moreover, these magnitudes continue to increase as the anchors are placed closer to the vicinity of loading, as shown in Fig. 15**(a)**, where the maximum strain magnitude was observed to be 0.0250. Therefore, when implanting/designing such strengthening configurations, it is important to be cognizant of the locations of these anchors to prevent significant stress concentrations that could otherwise result in local bearing or anchor shearing failures.

The strain contour in the y direction was also extracted, as shown in Fig. 15**(b)**, where the strain magnitudes were higher in the top of the anchors than the bottom, unlike what was observed in Fig. 15**(a)**. However, these values were way lower than those observed in Fig. 15**(a)** where the maximum tensile strain magnitude was 0.00350, smaller by a factor of ~ 10. In addition, the anchor exhibits a maximum compression at the extreme bottom; indicating that they are behaving like fixed beam elements where the point at which the AA plate is bearing against causes the EAB region at fixture to pull out. This mechanism results in tensile strain at the region of fixture and compression due to AA plate bearing. Similar to the plot in Fig. 15**(a)**, these stresses increase

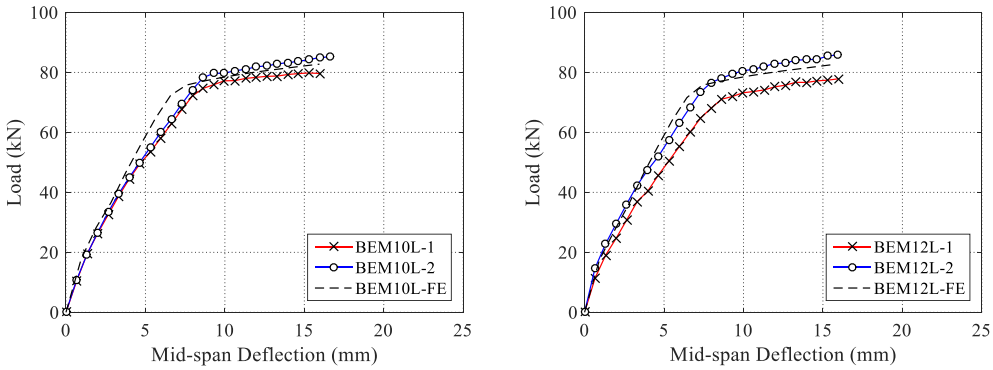

(d) Specimens BEM10L and BEM12L.

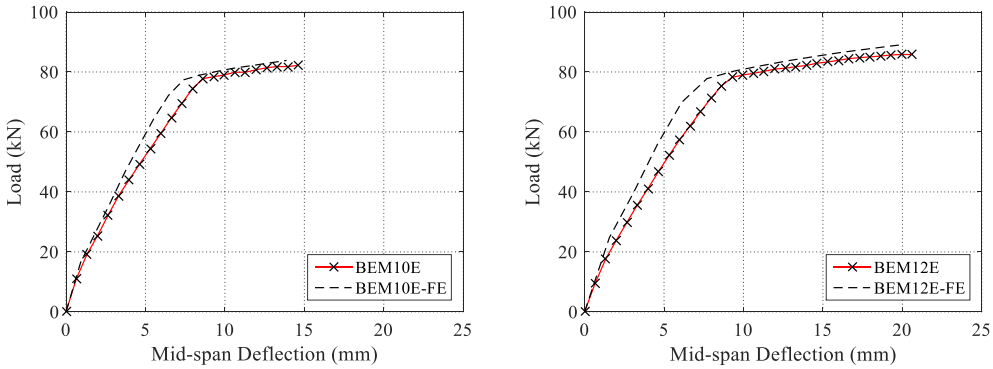

(e) Specimens BEM10L and BEM12L.

Fig. 13 (*continued*)

as the anchors get closer to the vicinity of loading, as shown in Fig. 15**(b)**.

Furthermore, concrete crack distribution at the bottom view of model BEM12E-FE was extracted to investigate the effect of implementing anchors on concrete crack propagation, as shown in Fig. 16. It is worth mentioning that the red and blue colored dots represent the first and second cracks, respectively, where the first crack results from concrete reaching its tensile strength at a given loading and the second crack results in the first cracks widening due to increased loading. It can be observed that most of model BEM12E-FE is covered with red dots at the extreme bottom fibers since the concrete elements have reached their tensile strength at maximum loading. However, at the locations of the anchors, green colored dots are also visible which indicate that concrete crack widen within the vicinity of the anchors. Similar observations were reported during the experiment [26,27].

6. Anchorage contribution

Fig. 15 shows the shear stress distribution along the X-Z plane between the soffit of the concrete beam and top of the AA plate. For brevity, only models BM10H-FE, BEM10H-FE, and BEM10L-FE were selected since these models capture the underlying differences in the anchorage systems. Model BM10H-FE demonstrated the largest shear stress concentrations at the end-EAB compared to the rest of the selected models, as shown in Fig. 15. This indicated that the absence of epoxy forced the EAB to engage in maintaining the plate from exhibiting EPD and increasing its susceptibility to EAB-shearing in strengthening applications involving stronger composite material (i.e., Carbon FRP composites). However, models BEM10H-FE and BEM10L-FE demonstrated uniform shear stress distribution between the EAB and epoxy elements, as shown in Fig. 15**(b) and (c)**, indicating increase engagement of the anchorage system prior to failure.

7. Parametric study

7.1. FE model matrix

The validated FE models were extended to conduct a parametric study to investigate the effect of varying the steel bar diameter on three selected FE models (CB-FE, CBE-FE, and BEM12E-FE) and increasing the AA plate grades on two selected FE models (CBE-FE and BEM12E-FE) on the strength and ductility of the strengthened models. The purpose of selecting model CB-FE was to provide a benchmark for the strength gain and ductility of models CBE-FE and BEM12E-FE. Table 5 presents the test matrix used during the parametric study where the prefixes "XX-FE", "XXmm", and "AAXXXX" refer to the FE model, steel bar diameter, and AA plate grade used, respectively, and ρ_s refers to the ratio of bottom longitudinal reinforcement. The steel bars' diameters varied between 10 and 16 mm and the aluminum grades used were AA5083, AA6061, and AA7075 where their grades were obtained from Max Steels [39], as shown in Table 5, with an elastic modulus of 70 GPa for all AA plate grades. For example, BEM12E-FE-12 mm refers to model BEM12E-FE reinforced with 12 mm steel bars and CBE-FE-AA6061 refers to model CBE-FE externally strengthened with an AA6061 plate. It is worth mentioning that a design check was carried out for models CB-FE-10 mm, CB-FE-12 mm, CB-FE-14 mm, and CB-FE-16 mm to maintain flexural deficiency in all of the un-strengthened models, as per the design criteria imposed by ACI 318–19 guidelines [34].

Table 4
Comparison between the FE predicted and selected experimental results.

Specimen	FE Model	Peak Load (kN)		|% Error|	Maximum Deflection (mm)		|% Error|	Failure Modes[a]	
		Experimental	FE		Experimental	FE		Experimental	FE
CB	CB-FE	64.2	60.2	6.23	17.4	17	2.3	SY, CC	SY, CC
CBE	CBE-FE	84.4	84	0.47	14.3	13.8	3.5	SY, CC, EPD	SY, CC, EPD
BEM10H	BEM10H-FE	83.5	80.9	3.11	15.5	15.1	2.58	SY, CC, PR	SY, CC, PR
BEM10L	BEM10L-FE	82.9	82.7	0.24	16.5	16	3.03	SY, CC, PR	SY, CC, PR
BM10H	BM10H-FE	76.9	72.8	5.33	17.1	16.2	5.26	SY, CC, PR	SY, CC, PR
BEM10E	BEM10E-FE	82.6	83.8	1.45	14.9	13.9	6.71	SY, CC, LPD	SY, CC, LPD
BEM12H	BEM12H-FE	84.2	82.2	2.38	18.7	17.7	5.35	SY, CC, PR	SY, CC, PR
BEM12L	BEM12L-FE	82.2	82.6	0.49	16.3	15.6	4.29	SY, CC, PR	SY, CC, PR
BM12H	BM12H-FE	83.6	79.6	4.78	19.9	19.9	0	SY, CC, PR	SY, CC, PR
BEM12E	BEM12E-FE	86.1	88.9	3.25	21	19.7	6.19	SY, CC, LPD	SY, CC, LPD

[a] : SY = steel yielding; CC = concrete crushing; EPD = end-plate debonding; PF = plate rupture; LPD = local-plate debonding.

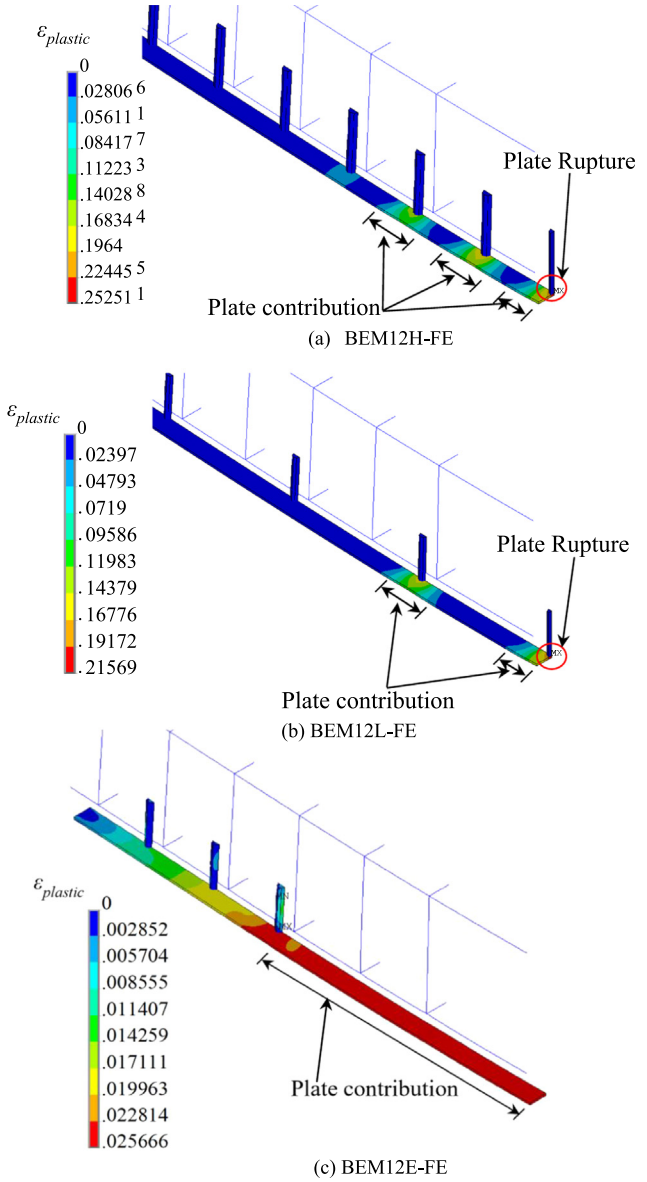

Fig. 14. First principal strain contour plots for selected FE models.

7.2. Effect of steel bar diameter on load–deflection response curves

Fig. 16 shows the load versus mid-span deflection curves for the models with different steel bar diameters. Model CB-FE responded positively with strength gains when the diameters of the steel bars increased, however, this allowed the model to fail at lower deformations due to significant crushing of concrete. This was also reported in a numerical study conducted by Hawileh et al. [29], where an increase in the steel bars' diameter increases the load-carrying capacity of the beam while reducing its ductility. In addition, all of the un-strengthened FE models demonstrated steel yielding (SY) followed by concrete crushing (CC)—according to the failure criteria defined previously in this paper.

On the other hand, model CBE-FE responded negatively in terms of both strength gain and ductility, as shown in Fig. 16**(b)**, due to EPD. It was observed that the increase in the steel bar diameter accelerated EPD failure modes at earlier stages of loading; thereby reducing the strength gain and ductility of the models. For example, models CBE-FE-10 mm and CBE-FE-12 mm exhibited + 38.6% and + 13.2% strength gains compared to models CB-FE-10 mm and CB-FE-12 mm, whereas models CBE-FE-14 mm and CBE-FE-16 mm exhibited −5.30% and −19.6% strength decay compared to models CB-FE-14 mm and CB-FE-16 mm. As mentioned earlier, the reduction in strength gain was also accompanied with a reduction in ductility, where models CBE-FE-10 mm, CBE-FE-12 mm, CBE-FE-14 mm, and CBE-FE-16 mm exhibited –22.8%, −45.9%, −43.5%, and −41.3% percentage ductility decay, respectively. This is clearly demonstrated when observing the curves for models with large steel bar diameters like CBE-FE-14 mm and CBE-FE-16 mm in which only a linear increase is shown as opposed to the curves of models CB-FE-14 mm and CB-FE-16 mm, shown in Fig. 16**(a)**, in which the curves plateau indicating a larger utilization of steel. The failure modes experienced by each model was SY followed by CC and EPD in models CBE-FE-10 mm and CBE-FE-12 mm, CC followed by EPD occurred in model CBE-FE-14 mm, and only EPD occurred in model CBE-FE-16 mm.

Fig. 16**(c)** shows that the implementation of EAB as end-anchors with epoxy allowed most of the models (BEM12E-FE-10 mm, BEM12E-FE-12 mm, and BEM12E-FE-14 mm) to maintain bi-linear behavior in load-carrying capacity similar to those in Fig. 16**(a)**. For example, models BEM12E-FE-10 mm, BEM12E-FE-12 mm, and BEM12E-FE-14 mm exhibited + 47.7%, +17.9%, and + 6.58% strength gains, respectively, whereas model BEM12E-FE-16 mm showed negligible strength gain. In addition, percentage deflection gain was observed for models BEM12E-FE-10 mm and BEM12E-FE-12 mm in which these models exhibited + 16.4% and + 10.9% deflection gain, whereas models BEM12E-FE-14 mm and BEM12E-FE-16 mm exhibited −6.60% and −12.0% deflection decay. Although the strength and ductility of the strengthened specimens are being reduced, the EAB in form of end-anchors minimized these drawbacks. The failure modes exhibited were SY followed by CC and LPD for models BEM12E-FE-10 mm, BEM12E-FE-12 mm, and BEM12E-FE-14 mm and CC followed by LPD for model BEM12E-FE-16 mm.

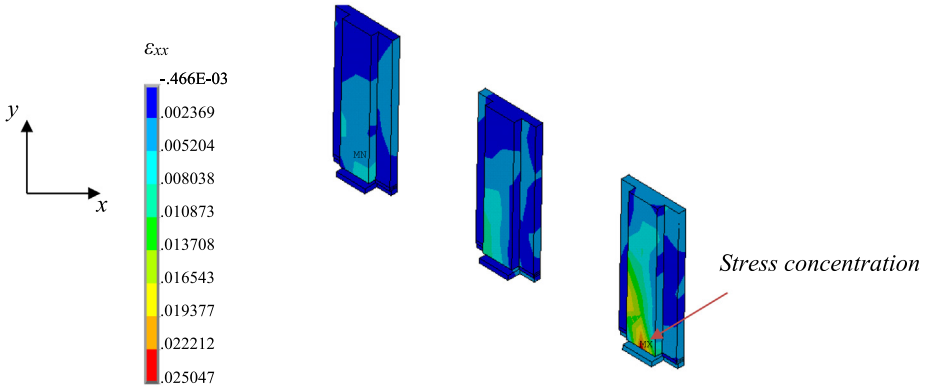

(a) X-component of strain distribution.

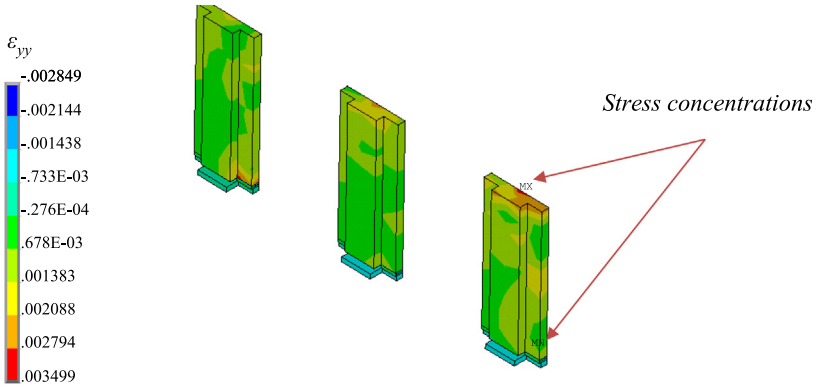

(b) Y-component of strain distribution.

Fig. 15. Local Strain Behavior of Model BEM12E-FE.

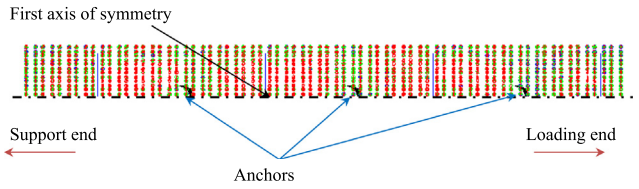

Fig. 16. Crack pattern of bottom view in model BEM12E-FE.

7.3. Effect of AA plate grade on load–deflection response curves

Fig. 17 shows the load versus mid-span deflection curves for externally strengthened FE models (CBE-FE and BEM12E-FE) with different AA plate grades. CB-FE-10 mm served as the control model for evaluating the strength gains and ductility gain/decay for the models in Fig. 17. In general, all of the models demonstrated an increase in strength and a decrease in ductility when larger AA plate grades were used. For example, models CBE-FE-AA5083, CBE-FE-AA6061, and CBE-FE-AA7075 exhibited + 38.6%, +50.1%, and + 55.3% strength gains, respectively, and –22.8%, −51.1%, and −54.5% ductility decay, respectively. The ductility is inadequate for the models with larger AA plate grades due to EPD at early stages of loading. In Fig. 17**(a)**, the CBE-FE models were terminated due to EPD failure in which SY followed by CC and EPD occurred in models CBE-FE-AA5083 and CBE-FE-AA6061, whereas only EPD occurred in model CBE-FE-AA7075.

On the other hand, the models in Fig. 17**(b)** exhibited larger strength gains and ductility when compared to the models in Fig. 17 (a). For example, models BEM12E-FE-AA5083, BEM12E-FE-AA6061, and BEM12E-FE-AA7075 exhibited + 47.7%, +54.4%, and + 69.3% strength gains, respectively, and + 16.4%, −3.76%, and −19.9% ductility gain/decay, respectively. Therefore, the implementation of EAB as end-anchors allowed the models to fully utilize the AA plates such that the models were capable of resisting loads at higher deformations that those in Fig. 17**(a)**. Unlike the increase in the diameter of the steel bars, the increase in the AA plate grade had a positive impact on the strength gain in the model BEM12E-FE.

7.4. Summary and discussion of results

A brief summary of the results discussed in the previous sections is shown in Table 6. It can be concluded that the reduction in strength gain and ductility due to the increase in steel bar diameter was minimized when EAB was used as end-anchors in RC beams strengthened with AA plates. Moreover, larger AA plate grades performed better in the model with EAB as end-anchors (BEM12E-FE) than the model strengthened with EB AA plates (CBE-FE). Fig. 18 summarized the findings of this parametric study where model BEM12E-FE outperformed model CBE-FE despite the

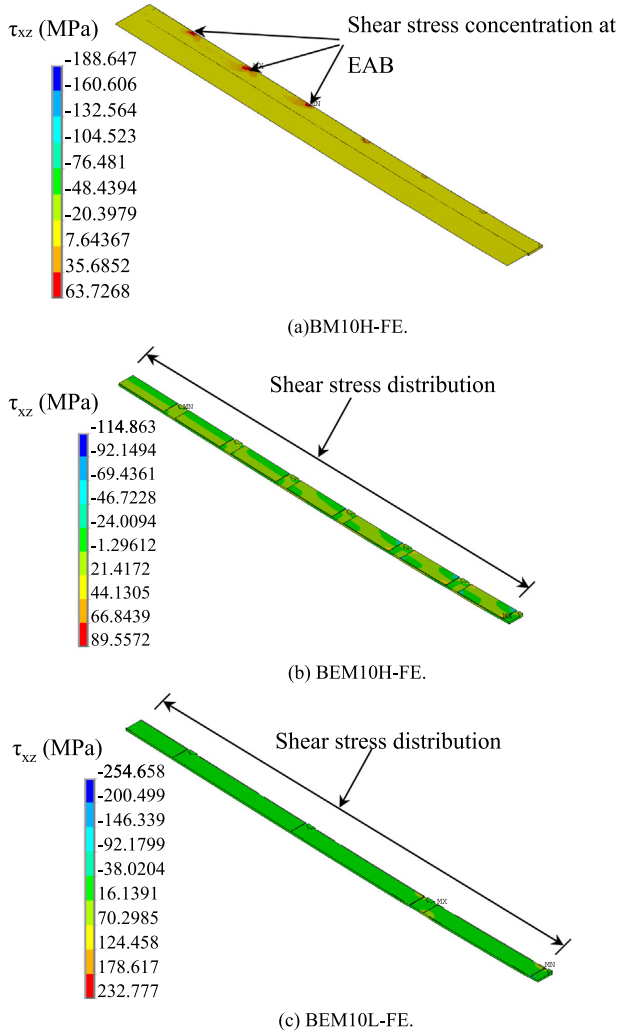

Fig. 17. Shear stress contour plots in the X-Z plane for selected FE models.

drawbacks associated with the increase in steel bar diameters or aluminum grades.Fig. 19.Fig. 20.

8. Summary and conclusion

This study focused on numerically modeling results of previous tests, carried out by the authors, to numerically investigate the effect of using mechanically fastened (MF) and externally bonded (EB) aluminum alloy (AA) plates on the flexural enhancement of RC beams. Detailed comparisons of load versus displacement curves, load versus strain curves, and failure modes were carried out against those observed during the test. This helped in validating the models and enabling the authors to further assess stress and strain propagations along the elements without the expense of conducting additional tests. Finally, a parametric study was carried out to study the effect of varying the steel bar diameters and AA plate grades on the flexural response of the models. The following conclusions can be drawn from this study.

1. Accurate material and element definitions allowed the FE models to simulate the flexural response observed in the experiment by means of reproducing relatively similar load versus displacement curves, load versus strain curves, and failure modes like end-plate debonding (EPD), local-plate debonding (LPD), and plate rupture (PR). As a result, the maximum deviation of the peak loads and deflection values were 6.23 and 6.12%, respectively, compared to those obtained from the experiment.
2. The inclusion of an interfacial bond stress-slip model between the AA plate and concrete elements during loading caused a rigid body motion to occur in the AA elements such that debonding was observed. This forced the analysis to terminate in a similar manner to what was observed in the tests.
3. The first principal strain contour plots revealed that a linear EAB layout can cause strain concentrations at the locations of the bolts where the maximum strain achieved was at the beam's mid-span, thus, indicating a PF failure.

Table 5
Test matrix used in parametric study.

Model Designation	Geometric Details (mm)		Reinforcement Details		AA Plate Details		
	Depth (mm)	Width (mm)	Bar diameter (mm)	ρ_s (%)	Thickness (mm)	Width (mm)	Grade (MPa)
CB-FE-10 mm	240	125	10	0.299	3	50	150
CB-FE-12 mm	240	125	12	0.431	3	50	150
CB-FE-14 mm	240	125	14	0.586	3	50	150
CB-FE-16 mm	240	125	16	0.766	3	50	150
CBE-FE-10 mm	240	125	10	0.299	3	50	150
CBE-FE-12 mm	240	125	12	0.431	3	50	150
CBE-FE-14 mm	240	125	14	0.586	3	50	150
CBE-FE-16 mm	240	125	16	0.766	3	50	150
BEM12E-FE-10 mm	240	125	10	0.299	3	50	150
BEM12E-FE-12 mm	240	125	12	0.431	3	50	150
BEM12E-FE-14 mm	240	125	14	0.586	3	50	150
BEM12E-FE-16 mm	240	125	16	0.766	3	50	150
CBE-FE-AA5083	240	125	10	0.299	3	50	150
CBE-FE-AA6061	240	125	10	0.299	3	50	275
CBE-FE-AA7075	240	125	10	0.299	3	50	503
BEM12E-FE-AA5083	240	125	10	0.299	3	50	150
BEM12E-FE-AA6061	240	125	10	0.299	3	50	275
BEM12E-FE-AA7075	240	125	10	0.299	3	50	503

Table 6
Summary of results.

Model Designation	Peak Load (kN)	Ultimate Deflection (mm)	Strength Gain/Decay (%)	Deflection Gain/Decay (%)	Failure modes
CB-FE-10 mm	60.2	17.0	–	–	SY, CC
CB-FE-12 mm	83.1	14.3	–	–	SY, CC
CB-FE-14 mm	109.2	11.7	–	–	SY, CC
CB-FE-16 mm	137.3	10.3	–	–	SY, CC
CBE-FE-10 mm	83.5	13.1	38.6	−22.8	SY, CC, EPD
CBE-FE-12 mm	98.3	7.7	18.2	−45.9	SY, CC, EPD
CBE-FE-14 mm	103.5	6.6	−5.3	−43.5	CC, EPD
CBE-FE-16 mm	110.3	6.1	−19.6	−41.3	EPD
BEM12E-FE-10 mm	89.0	19.8	47.7	16.4	SY, CC, LPD
BEM12E-FE-12 mm	98.0	15.9	17.9	10.9	SY, CC, LPD
BEM12E-FE-14 mm	116.4	10.9	6.58	−6.60	SY, CC, LPD
BEM12E-FE-16 mm	137.0	9.1	−0.21	−12.0	CC, LPD
CBE-FE-AA5083	83.5	13.1	38.6	−22.8	SY, CC, EPD
CBE-FE-AA6061	90.4	8.3	50.1	−51.1	SY, CC, EPD
CBE-FE-AA7075	93.5	7.7	55.3	−54.5	EPD
BEM12E-FE-AA5083	89.0	19.8	47.7	16.4	SY, CC, LPD
BEM12E-FE-AA6061	93	16.4	54.4	−3.76	SY, CC, LPD
BEM12E-FE-AA7075	102	13.6	69.3	−19.9	SY, CC, LPD

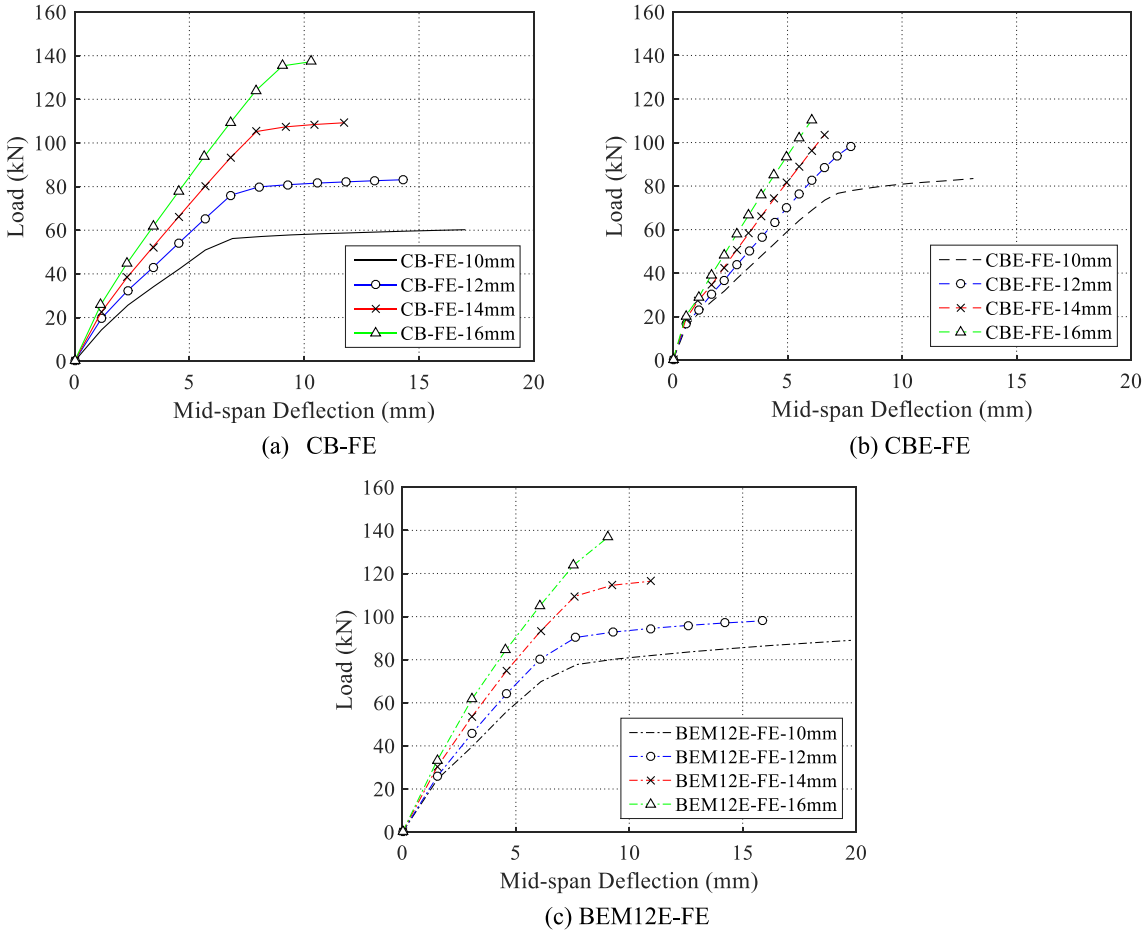

Fig. 18. Load versus mid-span deflection curves for models reinforced with different steel bar diameters.

4. During loading, strain propagations in the longitudinal × direction were observed to be maximum at the bottom of the EAB where the AA plate is located at, while the strain propagation in the vertical y direction was maximum at the top of the EAB within the concrete elements.
5. The EAB demonstrated beam-like behavior such that the anchor exhibited maximum compression and tensile strains at the bottom and top, respectively, of the anchors. This indicated that the anchors are behaving like fixed beam elements where the point at which the AA plate is bearing against causes the EAB region at fixture to pull out; resulting in tension at the top of the EAB and compression at the bottom.

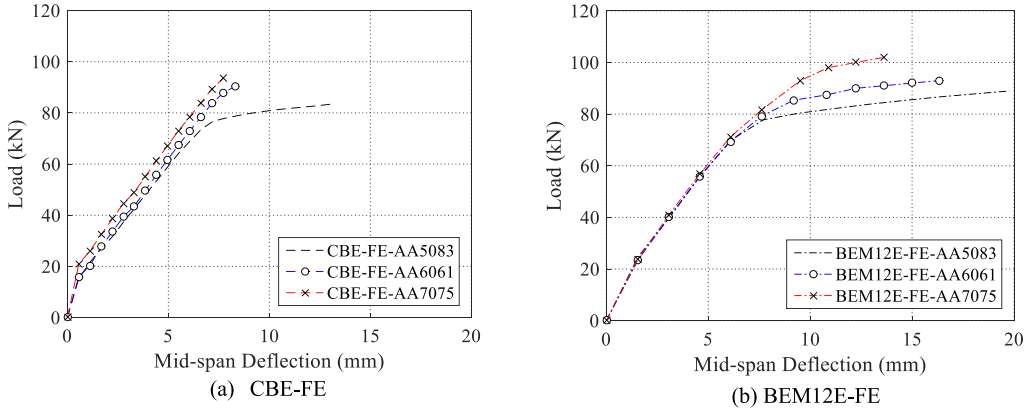

Fig. 19. Load versus mid-span deflection curve for models with different aluminum grades.

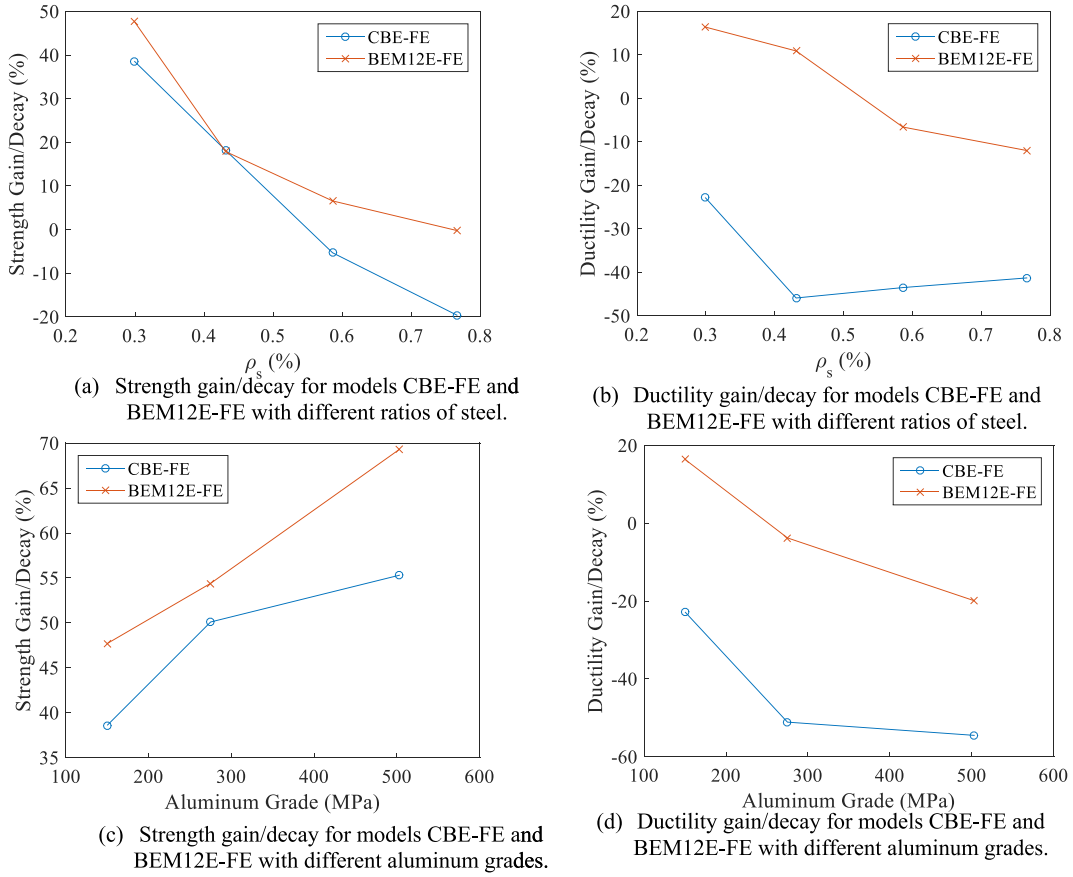

Fig. 20. Summary of relationships deduced during the parametric study.

6. Concrete cracks at the soffit of the beam tend to widen at the vicinity of anchors during maximum loading.
7. The model consisting of EAB as end-anchors demonstrated large strain distributions along the un-anchored length of the AA plate in which the segment within the vicinity of the loading plates was significantly utilized at ultimate loading conditions.
8. Using epoxy with EAB helped in enhancing the anchorage system such that the shear stress concentrations at the plane within the epoxy elements were re-distributed between the EAB and epoxy elements. On the other hand, the models strengthened with only MF AA elements experienced shear stress concentrations on the location of the bolts at the ends of the plates. Therefore, RC beams strengthened with larger grades will require more EAB with epoxy to avoid shearing of the EAB at ultimate loading conditions.
9. The strength gain and ductility of the models with increasing steel bar diameters varied depending on the failure modes exhibited. The models strengthened with EB AA plates demonstrated significant reduction in both the strength gain and ductility during loading, whereas the model strengthened with EAB as end-anchors and EB AA

plates showed less reduction in strength gain and ductility. Hence, shifting or postponing premature failure modes helped minimize the drawbacks demonstrated by a typically strengthened FE model with larger steel bar diameters.

10. The strength gain and ductility exhibited by the models with higher aluminum grades also varied depending on the failure mode observed. The model strengthened with EB AA plates demonstrated strength enhancements with poor ductility, whereas the models that were strengthened with EAB as end-anchors and EB AA plates demonstrated significant strength enhancements and ductility.

The FE models validated in the present study can serve as a reliable platform for researchers and engineers to simulate the nonlinear flexural behavior of RC elements strengthened with MF and/or EB AA plates. Moreover, the generated diagrams could assist researchers/engineers in determining a more efficient section when designing such retrofitted specimens. Future works to expand this study can be conducted by employing these FE models to perform more tests and investigate the effects of different parameters on their structural performance. The authors recommend testing parameters like varying the number, spacing, and grade of the EAB while adding or removing epoxy, and monitoring their effects on the flexural capacity, ductility, and failure mode of the FE models.

Declaration of Competing Interest

The authors declare that they have no known competing financial interests or personal relationships that could have appeared to influence the work reported in this paper.

Acknowledgements

The support for the research presented in this paper had been provided by Riad Sadek Endowed Chair in Civil Engineering at the American University of Sharjah. The support is gratefully appreciated and acknowledged. The views and conclusions, expressed or implied, in this study are those of the authors and should not be interpreted as those of the donor or the institution.

References

[1] Naser MZ, Hawileh RA, Abdalla JA. Fiber-reinforced polymer composites in strengthening reinforced concrete structures: A critical review. Eng Struct 2019;198(1):109542.
[2] Xu Q, Chen L, Han C, Harries KA, Xu Z. Experimental research on fire-damaged RC continuous T-beams subsequently strengthened with CFRP sheets. Eng Struct 2019;183(15):135–49.
[3] Bodzak P. Flexural behaviour of concrete beams reinforced with different grade steel and strengthened by CFRP strips. Compos B Eng 2019;167(15):411–21.
[4] Triantafyllou GG, Rousakis TC, Karabinis AI. Corroded RC beams patch repaired and strengthened in flexure with fiber-reinforced polymer laminates. Compos B Eng 2017;112(1):125–36.
[5] Song L, Yu Z. Fatigue performance of corroded reinforced concrete beams strengthened with CFRP sheets. Constr Build Mater 2015;90(15):99–109.
[6] Hawileh RA, Rasheed HA, Abdalla JA, Al-Tamimi AK. Behavior of reinforced concrete beams strengthened with externally bonded hybrid fiber reinforced polymer systems. Material Design 2014;53:972–82.
[7] Al-Zaid RZ, Al-Negheimish AI, Al-Saawani MA, El-Sayed AK. Analytical study on RC beams strengthened for flexure with externally bonded FRP reinforcement. Compos B Eng 2012;43:129–41.
[8] Salama ASD, Hawileh RA, Abdalla JA. Performance of externally strengthened RC beams with side-bonded CFRP sheets. Compos Struct 2019;212 (15):281–90.
[9] Abdalla JA, Hawileh RA, Nawaz W, Mohammed A. Reinforced concrete beams externally strengthened in flexure using hybrid systems. In: In: 2018 Advances in Science and Engineering Technology International Conferences -. p. 1–5.
[10] Abdalla JA, Abu-Obeidah AS, Hawileh RA, Rasheed HA. Shear strengthening of reinforced concrete beams using externally-bonded aluminum alloy plates: An experimental study. Constr Build Mater 2016;128(15):24–37.
[11] Abu-Obeidah A, Hawileh RA, Abdalla JA. Finite element analysis of strengthened RC beams in shear with aluminum plates. Comput Struct 2015;147(15):36–46.
[12] Abdalla JA, Hraib FH, Hawileh RA, Mirghani AM. Experimental investigation of bond-slip behavior of aluminum plates adhesively bonded to concrete. J Adhes Sci Technol 2017;31(1):82–99.
[13] Rasheed HA, Abdalla JA, Hawileh RA, Al-Tamimi AK. Flexural behavior of reinforced concrete beams strengthened with externally bonded Aluminum Alloy plates. Eng Struct 2017;147(15):473–85.
[14] Abuodeh OR, AlRifai M, Hawileh RA, Abdalla JA. Finite Element Modelling of Aluminum Alloy Plated Beams. In: In: 8th International Conference on Modeling Simulation and Applied Optimization -. p. 1–5.
[15] Mirghani AM, Abdalla JA, and Hawileh RA. Modeling and simulation of bond-slip behavior of Aluminum Alloy plates adhesively bonded to concrete. In: 2017 7th International Conference on Modeling, Simulation, and Applied Optimization - ICMSAO; 2017. p. 1–5.
[16] Hawileh RA, Nawaz W, Abdalla JA. Flexural behavior of reinforced concrete beams externally strengthened with Hardwire Steel-Fiber sheets. Constr Build Mater 2018;172(30):562–73.
[17] Hawileh RA. Finite element modeling of reinforced concrete beams with a hybrid combination of steel and aramid reinforcement. Mater Des 2015;65:831–9.
[18] Wan B, Jiang C, Wu YF. Effect of defects in externally bonded FRP reinforced concrete. Constr Build Mater 2018;172(30):63–76.
[19] El-Maaddawy TA. Mechanically Fastened Composites for Retrofitting Corrosion-Damaged Reinforced-Concrete Beams: Experimental Investigation. J Compos Constr 2013;18(2):04013041.
[20] Khan A, Ayub T. Effectiveness of U-shaped CFRP wraps as end anchorages in predominant flexure and shear region. In: In: the 5th International Conference on FRP Composites in Civil Engineering -. p. 533–6.
[21] Al-Tamimi AK, Hawileh RA, Abdalla JA, Rasheed HA. Effects of Ratio of CFRP Plate Length to Shear Span and End Anchorage on Flexural Behavior of SCC RC Beams. J Compos Constr 2011;15(6):908–19.
[22] Ali A, Abdalla JA, Hawileh RA, Galal K. CFRP mechanical anchorage for externally strengthened RC beams under flexure. Phys. Procedia 2014;55:10–6.
[23] Loring HB, Davids WG. Mechanically fastened hybrid composite strips for flexural strengthening of concrete beams. Constr Build Mater 2015;76 (1):118–29.
[24] El Maaddawy T, Soudki K. Strengthening of reinforced concrete slabs with mechanically-anchored unbonded FRP system. Constr Build Mater 2008;22 (4):444–55.
[25] El-Maaddawy T, Chekfeh Y. Retrofitting of Severely Shear-Damaged Concrete T-Beams Using Externally Bonded Composites and Mechanical End Anchorage. J Compos Constr 2012;16(6):693–704.
[26] Abuodeh OR, Abdalla JA, Hawileh RA. Experimental and numerical study of RC beams strengthened in flexure with bolted/bonded AA plates. American University of Sharjah; 2019.
[27] Abuodeh OR, Abdalla JA, Hawileh RA. The flexural behavior of bolting and bonding Aluminum Alloy plates to RC beams. Procedia Struct Integrity 2019;17:395–402.
[28] Camata G, Spacone E, Zarnic R. Experimental and nonlinear finite element studies of RC beams strengthened with FRP plates. Compos B Eng 2007;38 (2):277–88.
[29] Hawileh RA, Naser MZ, Abdalla JA. Finite element simulation of reinforced concrete beams externally strengthened with short-length CFRP plates. Compos Part B Eng 2013;45(1):1722–30.
[30] Hawileh RA. Nonlinear finite element modeling of RC beams strengthened with NSM FRP rods. Constr Build Mater 2012;27(1):461–71.
[31] Yanhua G, Binsong J, Xiuguang S. Experimental Study and Numerical Simulation on Bonding Behavior of the New HB-FRP Strengthening Technology. J Perform Constr Facil 2012;26(2):220–7.
[32] Sweedan AMI, Rojob HN, El-Sawy KM. Mechanically-fastened hybrid composites for flexural strengthening of steel beams. Thin-Walled Struct 2014;85:250–61.
[33] ANSYS Academic Research Mechanical, Mechanical APDL Documentation. 2019.
[34] ACI Committee 318, Building Code Requirements for Structural Concrete and Commentary. Farmington Hills, Michigan (USA): American Concrete Institute, 2019.
[35] Hognestad E, Hlanson NW, McHenry D. Concrete Stress Distribution in Ultimate Strength Design. ACI Journal Proc 1955:455–79.
[36] Willam KJ and Warnke ED. Constitutive Model for the Triaxial Behavior of Concrete. In: Proc. Int. Association for Bridge and Structural Engineering; 1975. p. 1–174.
[37] Lu XZ, Teng JG, Ye LP, Jiang JJ. Bond–slip models for FRP sheets/plates bonded to concrete. Eng Struct 2005;27(6):920–37.
[38] Abu-Obeidah A, Hawileh RA, Abdalla JA. Finite Element Modeling of Shear Deficient Beams Bonded with Aluminum Plates. In: In: Proceedings of the Eleventh International Conference on Computational Structures Technology. p. 1–8.
[39] Max Steel, "Aluminum Alloy Sheet & Plate," 2019. [Online]. Available: https://www.maxsteels.com/aluminium-alloy-products.html. [Accessed: 12-Aug-2019].